Science Bulletin 71 (2026) 1084–1092

Contents lists available at ScienceDirect

Science Bulletin

journal homepage: www.elsevier.com/locate/scib

Article

Spatial-adaptive active learning identifies ultra-durable and highly active catalysts for acidic oxygen evolution reaction

Bin Cao [c,1], Yin Qin [a,1,*], Yan Luo [c,1], Zhehan Ying [e], Zilin Yan [a], Lu-Tao Weng [e], Kaikai Li [d,*], Tong-Yi Zhang [b,c,*]

[a] School of Science, Harbin Institute of Technology, Shenzhen 518055, China
[b] Materials Genome Institute, Shanghai Frontier Science Center of Mechanoinformatics, and Center for Integrated Circuits and Advanced Display Materials, Shanghai University, Shanghai 200444, China
[c] Guangzhou Municipal Key Laboratory of Materials Informatics, Advanced Materials Thrust, Sustainable Energy and Environment Thrust, The Hong Kong University of Science and Technology (Guangzhou), Guangzhou 511400, China
[d] School of Materials Science and Engineering, Harbin Institute of Technology, Shenzhen 518055, China
[e] Material Characterization and Preparation Facility, The Hong Kong University of Science and Technology (Guangzhou), Guangzhou 511400, China

ARTICLE INFO

Article history:
Received 3 May 2025
Received in revised form 23 September 2025
Accepted 8 December 2025
Available online 15 December 2025

Keywords:
Spatial-adaptive
Active learning
Oxygen Evolution reaction
Stability
Multi-objective

ABSTRACT

Oxygen evolution reaction (OER) catalysts face a major challenge in the practical implementation of acidic water electrolysis for hydrogen production, primarily due to limitations in catalytic activity and stability. Despite extensive research, the development of acidic OER catalysts still relies largely on trial-and-error experimentation rather than AI-driven, target-oriented approaches. In this work, we address these limitations by introducing a spatial-adaptive active learning strategy integrated with closed-loop experimentation for targeted catalyst optimization in two stages. In the first stage, Bayesian optimization identifies highly active catalysts and a conditional variational autoencoder generates an adaptive low-overpotential subspace of stability candidates, while the second stage active learning finds the most stable catalyst within this subspace. Using this strategy, we discover a novel Cu-RuO_2 catalyst that exhibits remarkable stability for 625 h and an overpotential of 177 mV at a current density of 10 mA cm^{-2}. We provide detailed characterization and mechanistic insights into the newly discovered catalyst. Our study presents a transformative method for accelerating the design of stable acidic OER catalysts, thereby advancing the feasibility of large-scale green hydrogen production via acidic water electrolysis.

1. Introduction

Acidic water electrolysis is considered the most suitable technology by converting intermittent renewable energy into high-purity H_2, due to its inherent advantages over alkaline water electrolysis in terms of higher current density and instantaneous current response [1–9]. Although Ir-based catalysts are excellent for oxygen evolution reaction (OER), they are cost-prohibitive for large-scale industrial practice. In contrast, Ru-based oxides emerge as promising alternatives, reducing costs by a factor of 7.5, yet their suboptimal activity and stability, particularly their limited stability of only dozens of hours in acidic electrolytes, hinder practical application [10–14]. Currently, strategies to enhance OER performance encompass the use of multimetal oxides, doping, engineering defects, and optimizing composition and so on [10,15–23]. Beyond conventional catalyst design, machine learning (ML) has been used to accelerate experimental design [24–26]. For example, Wang et al. [24] integrated multi-source data and employed the sure independence screening and sparsifying operator (SISSO) method to develop a descriptor of perovskite OER catalyst activity and accordingly, subsequent experimental validation identified an optimal catalyst with an overpotential of 304 mV at 1 mA cm^{-2}. Similarly, Jiang et al. [25] applied a random forest model to establish predictive relationships between catalyst composition, morphology, phase, electrolyte pH, working electrode type, and OER overpotential. Their screening approach successfully identified a catalyst with an overpotential of 226 mV at 10 mA cm^{-2}. Moon et al. [26] utilized graph-based crystal structure embedding and active learning to optimize overpotentials, leading to the discovery

* Corresponding authors.
E-mail addresses: qinyin@hit.edu.cn (Y. Qin), likaikai@hit.edu.cn (K. Li), mezhangt@hkust-gz.edu.cn (T.-Y. Zhang).
[1] These authors contributed equally to this work.

https://doi.org/10.1016/j.scib.2025.12.021

of a $Ca_{0.8}Pr_{0.2}Co_{0.8}Fe_{0.2}O_{3-\delta}$ perovskite with the overpotential of 391 mV at 10 mA cm^{-2}. However, the stability of the discovered catalysts has not yet been reported [24–26]. Manu et al. [27] applied a multi-phase active learning strategy that sequentially considers catalyst composition, reaction condition and the multi-objective properties of alcohol synthesis catalysts. This sequential approach facilitates the exploration of a larger feature space while maintaining higher efficiency. Although ML and active learning have been employed in the investigation of OER catalysts, few studies have successfully achieved simultaneous optimization of both activity and stability. For industrial applications of Ru-based oxide catalysts, long-term stability and low overpotential at a given current density are the two critical factors [8,28–30]. The catalytic activity, i.e., the overpotential, can be rapidly assessed within minutes using linear sweep voltammetry (LSV), while evaluating stability is a long-term process. Simultaneously optimizing both stability and activity through the conventional active learning requires extensive time due to the need for iterative experimental validation of stability. Therefore, developing an active learning strategy to minimize the number of stability tests is crucial for discovering outstanding catalysts.

In this study, we propose a novel spatial-adaptive active learning strategy using a two-stage sequential optimization approach. This method connects multi-stage optimization through a conditional search space construction, sequentially optimizing multiple objectives and linking them via adaptive space generation. It effectively addresses the challenge of unequal-cost, multi-target active learning scenarios. The first stage adopts seven classical ML models and three acquisition functions to minimize overpotential (a lower-cost target) without considering stability (a higher-cost target) by selecting the optimal catalyst composition and synthesis conditions (see Methods). Four iterations of global Bayesian optimization expand the experimental dataset from the initial 8 samples to 20 samples. Next, a conditional variational autoencoder (CVAE) is applied to the labeled 20 samples. Using a pre-set overpotential threshold of 200 mV (a tunable hyperparameter), the CVAE generates a "low-overpotential" feature subspace of 785 samplecandidates from the full space of 19,200 candidates. Stability tests are performed on 8 samples with overpotentials below a threshold and the results form an initial dataset for the second stage of active learning, which focuses on discovering the best catalyst (high-stability) within the refined 785-candidate subspace. After three iterations of active learning, each involving the synthesis and testing of a single new catalyst, the design target is achieved with a newly identified catalyst. As illustrated in Fig. 1, the proposed spatial-adaptive active learning strategy synthesizes 23 samples in total while conducting only 11 stability tests, saving at least 12 stability tests and approximately 4734 testing hours, based on the average stability test duration, significantly accelerating materials discovery. Down to the earth, a novel Cu-doped RuO_2 catalyst with significantly enhanced stability and activity has been discovered, demonstrating remarkable stability of 625 h and an overpotential of 177 mV at 10 mA cm^{-2} in the chemical system [31]. Significantly, the stability of this catalyst outperforms that of prior Cu-RuO_2 catalysts by a factor of 78, with the latter demonstrating merely 8 h of stability and an overpotential of 188 mV under analogous conditions [21]. The results prove that the proposed spatial adaptive active learning approach is a powerful method for multi-objective optimization, especially for these objectives tested, at least in a partial sequential manner. In such circumstances, active learning in the first stage can be conducted on some objectives characterized by fast tests and hence a much smaller search space, with maximal (or minimal) acceptable values of the first optimized objectives, is constructed for the second stage of active learning on other objectives characterized by long-term tests.

2. Methods

2.1. Chemicals and materials

Ruthenium chloride hydrate ($RuCl_3{\cdot}xH_2O$, 35.0%–42.0% Ru basis), $H_2^{18}O$ solution (97 at% ^{18}O), ruthenium oxide (RuO_2), 5 wt% Nafion® solution, carbon nanotubes (CNTs) and copper oxide nanoparticles (CuO, 50 nm) were sourced from Aladdin Reagent (Shanghai) Co., Ltd. Sulfuric acid (H_2SO_4) and Ethanol (C_2H_5OH) were procured from Sinopharm Co., Ltd. All reagents were used directly without any additional purification or treatment.

2.2. Preparation of the Cu-RuO_2 nanoparticles

25 mg of CuO nanoparticles were suspended in 10 mL of deionized water with stirring for 10 min. Subsequently, 30 mg of $RuCl_3{\cdot}xH_2O$ (AR grade) were dissolved in deionized water to form a homogeneous solution, which was then added to the CuO suspension at 25 °C and continuously stirred for 24 h. The Cu-RuO_2 precursors were retrieved by filtration and rinsed three times with deionized water. Following drying under infrared light, the Cu-RuO_2 nanoparticles were synthesized through subsequent calcination in air.

2.3. Active learning

The active learning strategy follows a two-step process. In the first step, four iterations are performed, each providing three recommendations. An active learning loop optimizes the overpotential values. In each iteration, seven ML models are evaluated using leave-one-out cross-validation (LOOCV): Gaussian process regression (GPR), ridge regression (Ridge), lasso regression (Lasso), decision tree (DT), random forest (RF), gradient boosting regressor (GB), and support vector regression (SVR). The best model is integrated into the Bgolearn framework and used for utility value calculation for all candidates defined by orthogonal design [32].

The orthogonal search space is designed as: (1) volume of $RuCl_3$ (V_{Ru}) solution: 0.5 to 2 mL, in 0.1 mL increments; (2) volume of deionized water (V_{H_2O}): 5 to 30 mL, in 5 mL increments; (3) calcination temperature: 250 to 850, in 25 °C increments; (4) calcination time: 1 to 8 h, in one hour increments. This results in a total of 19,200 potential recipes. These recommendations are generated using predictive entropy search (PES) [33], expected improvement (EI) [34], and knowledge gradient (KG) [35] utility functions, implemented through the Bgolearn package.

In the second step, an adaptive virtual space is generated by the CVAE network (see Supplementary material), which includes 785 candidates. This stage employs an active learning loop using the KG utility function. The utility function accounts for model differences due to noisy observations and selects candidates with the highest expected improvement. The three iterations in this stage yield a satisfactory catalyst, with an overpotential of 177 mV and stability of 625 h.

3. Results

3.1. Spatial-adaptive active learning

The study aims to identify the most effective acidic OER catalyst with high stability and low overpotential by doping Cu into RuO_2, which is achieved through a templating method involving CuO nanoparticles (particle size: 50 nm), substitution of Cu ions with aqueous Ru ions, and subsequent calcination in air. Four key features influence the synthesis: V_{Ru}, V_{H_2O}, T, and t, while the mass of CuO was fixed at 25 mg for all experiments, thus ensuring Cu doping in all ML-optimized catalysts. These parameters define a

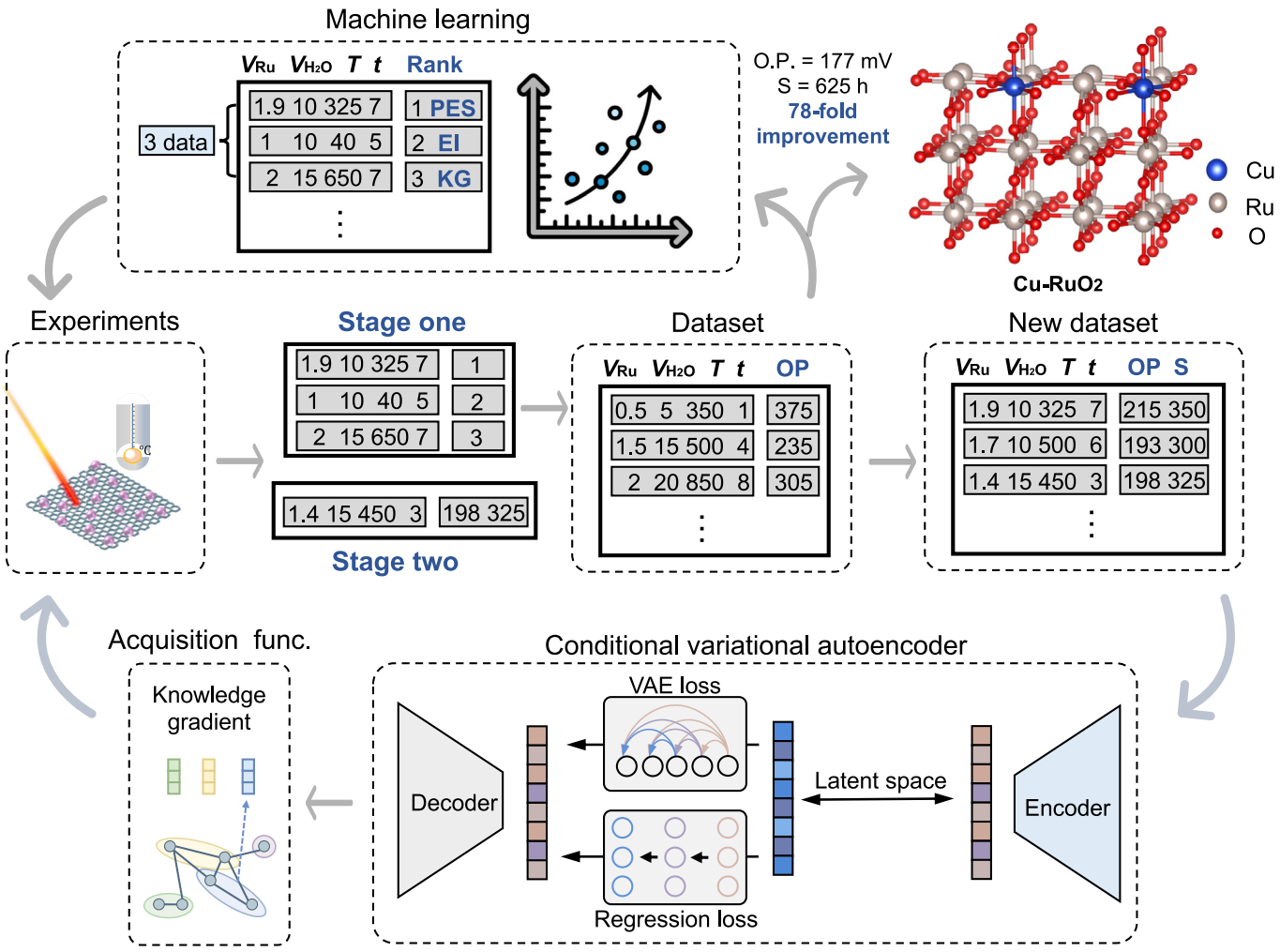

Fig. 1. The workflow of the spatial-adaptive active learning strategy. The workflow consists of two stages. In the first stage, overpotentials are optimized using active learning and hence the CVAE generates an adaptive sub-searching space constrained within the low-overpotential domain. In the second stage, active learning optimizes stability within the generated sub-searching space to identify ultra-durable and highly active catalysts. PES, EI, and KG denote predictive entropy search, expected improvement, and knowledge gradient, respectively. Func.: function.

four-dimensional feature space with a total of 19,200 possible candidates (see Methods). It is challenging to evaluate overpotential and stability simultaneously, as overpotential can be measured rapidly while stability assessment is inherently slow. To accelerate the overall discovery process, we propose a spatial-adaptive active learning strategy that operates in two sequential stages.

3.2. The first optimization stage and the CVAE network

Eight orthogonally designed catalysts are synthesized, and their overpotentials are measured, forming the initial dataset (Table S1 online). Seven ML algorithms are employed (see Methods). Except for Gaussian process regression, all other ML models are combined with the bootstrap sampling to provide statistical predictions. Three acquisition functions, PES, EI, and KG, are used in the first stage of active learning to select promising catalysts with low overpotentials from a search space of 19,200 candidates. Over four active learning iterations, three catalysts per iteration are added to the dataset, totaling 12 new catalysts (Table S2 online). Fig. 2a depicts the first stage of active learning, where newly measured overpotentials are added to the training dataset after each iteration. Overpotentials decrease over the first three iterations but slightly rise in the fourth, suggesting that the lowest value occurs at the third iteration (Fig. 2b) and indicating the terminal of iterations as well.

At each iteration, seven ML models are evaluated using LOOCV. The model with the lowest LOOCV mean squared error (MSE) is chosen as the surrogate model for candidate selection. Fig. 2c compares ML model performance in the fourth iteration (additional comparisons in Figs. S1, S2 online). MSE decreases across iterations, reaching its minimum in the fourth. By the end of stage one, 20 catalysts in total have been synthesized with the measurement of their overpotentials. The Synthetic Minority Oversampling Technique (SMOTE) is applied [36] to augment the dataset of 20 samples to 240 and the 240 labeled samples are fed into the CVAE network, where the feature vector is the direct input and the overpotential is used as the condition. The CVAE network consists of a self-attention-based encoder and a supervised decoder (see Supplementary material) as shown in Fig. 2d. The encoder maps the features into a latent space, where the condition is added, while the decoder reconstructs features back based on the desired design target. The generated candidate features, originally expressed as continuous variables, are assigned to the nearest predefined grid points in the orthogonal design search space. The training minimizes two key losses: (1) variational reconstruction loss, ensuring continuity in the latent variable distribution, and (2) design target loss, ensuring that the overpotentials of generated catalysts are consistent with the labeled ones. To generate the desired sub-candidate domain, experimentally observed data from Table S3

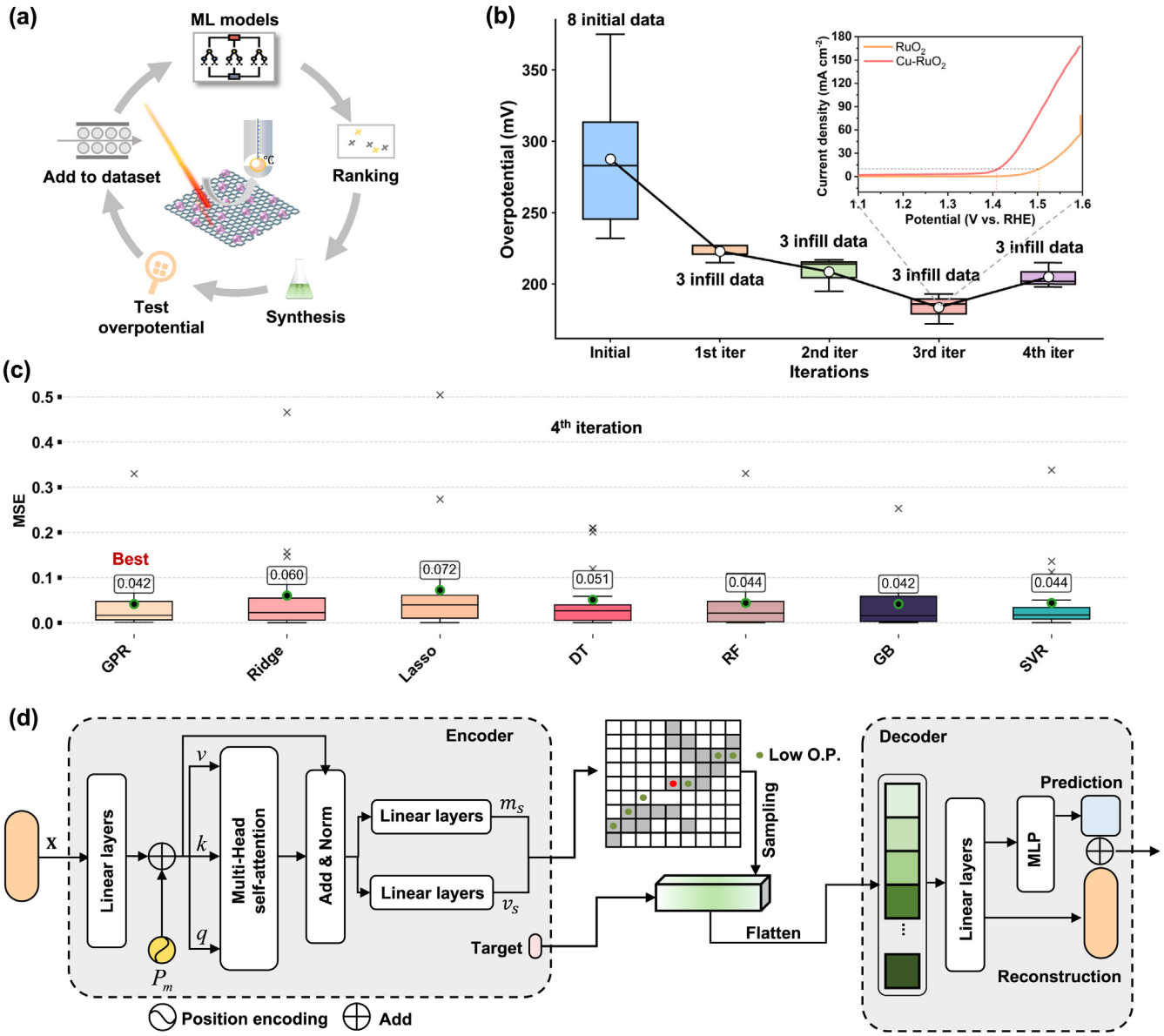

Fig. 2. Stage one optimization. (a) The active learning loop in stage one optimizes the overpotential. (b) The optimization trace over four iterations, with the inset illustrating the OER performance graph of the catalyst exhibiting the lowest overpotential. (c) Comparison of the MSE across various models at the fourth (final) iteration, evaluated using LOOCV. The models include GPR, Ridge, Lasso, DT, RF, GB, and SVR. Normalization is performed in each iteration. (d) The architecture of the CVAE network includes a self-attention-based encoder and a supervised decoder. The training loss of the network is derived from both the original VAE loss and the conditional prediction loss.

(online) are mapped into the latent space, where their distributions are labeled with overpotentials. Sampling from the one-sigma region of the latent space's multivariate Gaussian distribution focuses on recipes with overpotentials below 200 mV. These samples are then decoded back into the feature space, generating 785 virtual recipes. This approach significantly reduces the original search space of 19,200 candidates while introducing the low-overpotential constraint. Fig. S3 (online) presents the *t*-SNE (*t*-distributed stochastic neighbor embedding) plot [37] of generated recipes in the latent space, showing that recipes with lower overpotentials cluster in specific regions.

3.3. The second optimization stage and the OER performance

Among the 20 catalysts, 9 low-overpotential samples are selected, as listed in Table S3 (online). The stability tests are conducted on the 9 samples and by accident one sample is damaged. Thus, the initial dataset for stability active learning includes 8 samples only. Fig. 3a illustrates the second stage of the active learning process, which employs the GPR model and the KG acquisition function. The feature search space is confined to the 785 preselected feature points with low overpotentials. Experimental assessments then focus on measuring stability, with each iteration focusing on the evaluation of a single new catalyst candidate. Three optimization iterations were conducted, the optimal catalyst was identified in the second iteration with the features: V_{Ru} = 1.9 mL, V_{H_2O} = 5 mL, T = 350 °C and t = 8 h. However, under these synthesis conditions, the preparation of a pure RuO_2 catalyst was not feasible, suggesting the use of commercial RuO_2 for comparison. Fig. 3b presents experimental validation data from three iterative experiments, highlighting the optimized catalyst (named as Cu-RuO_2) with a Cu loading of about 4.6 wt% (as determined by

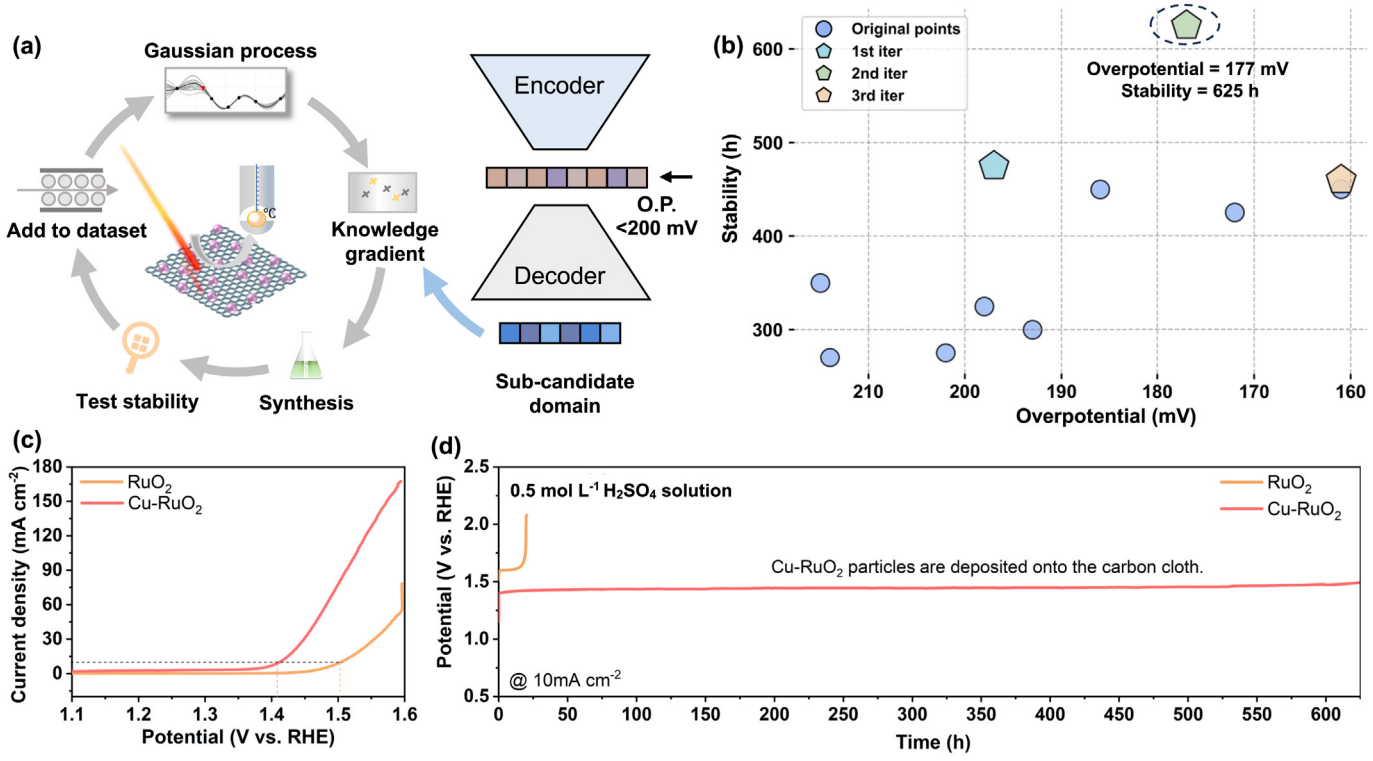

Fig. 3. Stage two optimization. (a) The active learning loop in the second stage searches for long stability from the search subspace of low overpotential, generated by CVAE. (b) The iteration trace shows each recommended datum per iteration. After three iterations, an outstanding electrocatalyst is synthesized, indicated by the marked dot cycle. (c) Representative LSV curves of commercial RuO_2 and Cu-RuO_2 in 0.5 mol L^{-1} H_2SO_4 solution. (d) Chronopotentiometric response of the commercial RuO_2 and Cu-RuO_2 at 10 mA cm^{-2}.

inductively coupled plasma-mass spectrometry, ICP-MS) prepared using the abovementioned optimal features.

The OER performance of the Cu-RuO_2 was systematically assessed in acidic media and compared with a commercial RuO_2 catalyst. Fig. 3c shows the LSV curves normalized to the geometric surface area of the working electrode. These results indicate that Cu-RuO_2 requires an overpotential (η_{10}) of only 177 mV to achieve a current density of 10 mA cm^{-2}, significantly lower than that of commercial RuO_2 (273 mV). Furthermore, as shown in Fig. S4 (online), Cu-RuO_2 exhibits a Tafel slope of 73.1 mV dec^{-1}, which is notably lower than that of commercial RuO_2 (99.0 mV dec^{-1}). The lower Tafel slope indicates enhanced OER kinetics of the Cu-RuO_2 catalyst [38]. The electrochemically active surface area (ECSA), estimated from double-layer capacitance (C_{dl}) measurements via cyclic voltammetry (CV) at varying scan rates (Figs. S5, S6 online), further highlights the superior performance of the Cu-RuO_2 catalyst. With a C_{dl} of 48.4 mF cm^{-2} and an ECSA of 97.57 cm^2, Cu-RuO_2 significantly outperforms commercial RuO_2 (C_{dl} = 18.8 mF cm^{-2}, ECSA = 37.9 cm^2). This difference highlights the role of the unique morphology, crystal structure, and Cu doping, which was synthesized using an ML-optimized protocol, in exposing more abundant active sites compared to commercial RuO_2, thereby enhancing the OER activity in acidic media. Fig. 3d compares the stability of the two catalysts under acidic OER conditions. In contrast to commercial RuO_2, which degrades rapidly within 15 h, the Cu-RuO_2 catalyst exhibits remarkable stability, maintaining consistent performance for over 625 h at a current density of 10 mA cm^{-2}. This stability represents a 78-fold improvement over previously reported Cu-doped RuO_2 [21]. Additionally, as demonstrated in Fig. S7 (online), Cu-RuO_2 exhibits stable operation for at least 200 h at 100 mA cm^{-2}, further highlighting its significant potential for practical application in water electrolysis. Combined with its outstanding activity, the Cu-RuO_2 emerges as a superior catalyst among most reported Ir/Ru-based systems for the acidic OER, as summarized in Fig. S8 and Table S5 (online) [6,8,15,18,19,21,38–51].

4. Crystal structure and ML interpretive analysis of the Cu-RuO_2

Transmission electron microscopy (TEM) images (Fig. 4a, b and Fig. S9 online) reveal that Cu-RuO_2 is composed of secondary particles formed by sub-5 nm nanoparticles, exhibiting a microsphere morphology with high surface roughness. In contrast, commercial RuO_2 exhibits sharply defined crystallites exceeding 100 nm in size with comparatively smooth surfaces (Fig. S10 online). Fig. 4b shows lattice fringes corresponding to the RuO_2 (110) and (101) planes in Cu-RuO_2, with lattice spacings of 3.16 and 2.50 Å, respectively. These values are smaller than those of commercial RuO_2 (110): 3.18 Å; (101): 2.56 Å (Fig. S11 online), suggesting lattice compression in Cu-RuO_2. The XRD patterns of commercial RuO_2 and Cu-RuO_2 were analyzed using our in-house developed software PyWPEM (https://github.com/Bin-Cao/PyWPEM) via Rietveld refinement, further showing a rutile-type structure with broadened diffraction peaks shifted toward higher angles (Fig. 4c and Tables S6–S8 online). This peak broadening and angular shift indicate a reduced RuO_2 lattice spacing and smaller crystallite size, consistent with structural modifications resulting from the unique synthesis process based on ML-optimized (V_{Ru}: 1.9 mL; V_{H_2O}: 5 mL; T: 350 °C; t: 8 h). Extended X-ray absorption fine structure (EXAFS) analysis of Ru K-edge (k^2-weighted) was performed to uncover the local atomic environment of Cu-RuO_2 (Fig. 4d). The peak at 1.47 Å corresponds to the first-shell Ru–O interactions, while the peak at 3.1 Å is linked to the second-shell Ru–Ru interactions [15,19,52]. After phase correction, the Ru–O and Ru–Ru distances are refined

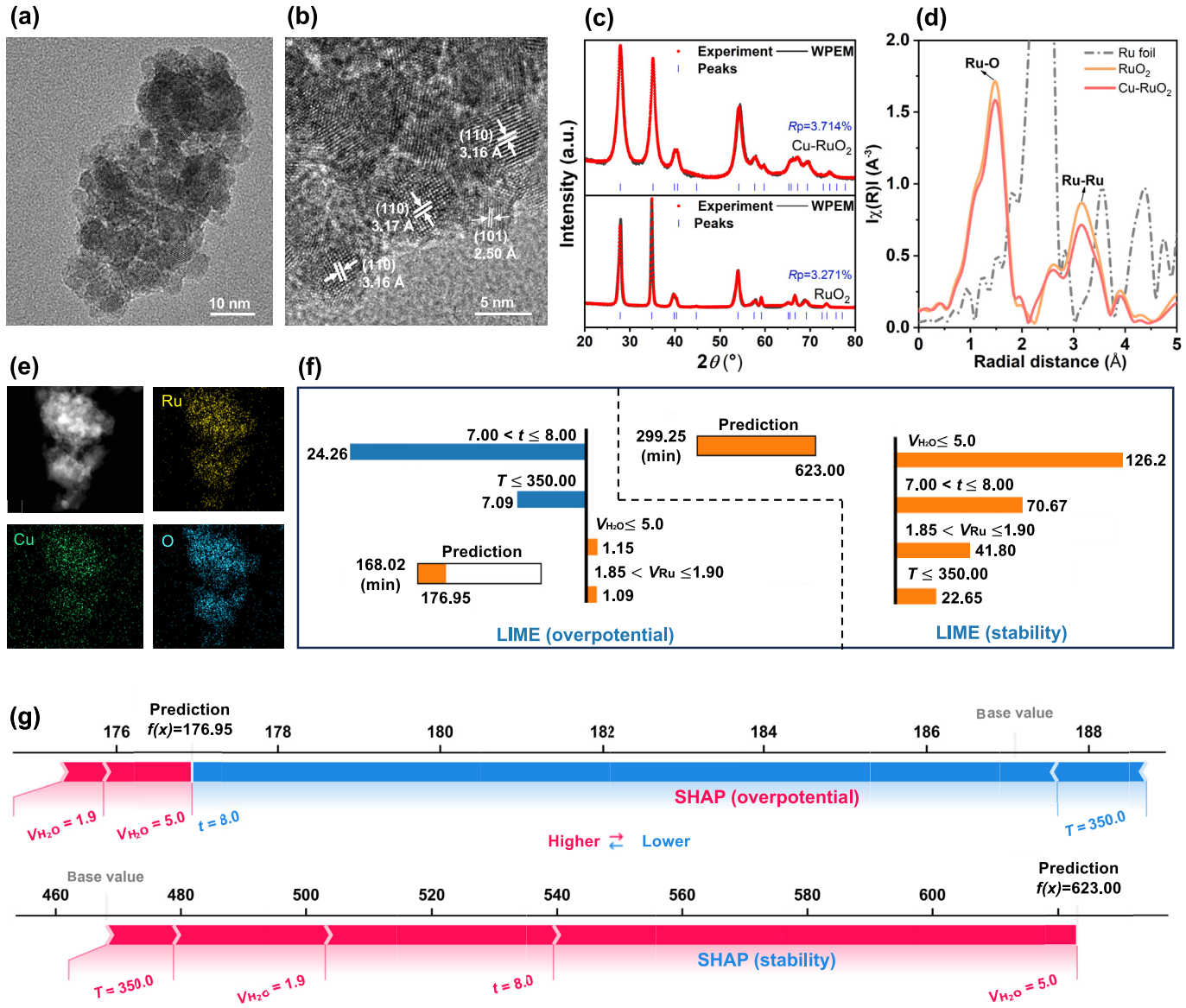

Fig. 4. Crystal structures and OER performance. (a) TEM image of Cu-RuO_2. (b) HRTEM image of Cu-RuO_2. (c) The refined XRD patterns of commercial RuO_2 and Cu-RuO_2. (d) Fourier transformed Ru K-edge EXAFS spectra of Ru foil, commercial RuO_2 and Cu-RuO_2. (e) TEM image of the Cu-RuO_2, and the corresponding EDS element distribution of Ru, Cu, and O. (f) LIME interpretive analysis of feature contributions to the catalyst's high activity and stability properties. (g) SHAP interpretive analysis of feature contributions.

to 1.81 and 3.44 Å, respectively. For Cu-RuO_2, both Ru–O and Ru–Ru bond lengths are noticeably shortened compared to commercial RuO_2, further reflecting the lattice compression. Furthermore, the reduced intensity of Ru–Ru/O peaks in Cu-RuO_2 suggests a lower Ru coordination number, indicative of coordination deficiency in Cu-RuO_2. This result is further supported by the wavelet transform (WT) analysis of the Ru K-edge EXAFS signals and the phase-corrected EXAFS of the Ru K-edge (Figs. S12–S14 online). Reduced nanoparticle size and a higher density of defects generally contribute to increased exposure of active sites, which is consistent with the ECSA results discussed earlier for commercial RuO_2 and Cu–RuO_2, thereby enhancing the OER activity. Energy-dispersive spectroscopy (EDS) mappings (Fig. 4e) confirm the homogeneous distribution of Ru, Cu, and O, indicating uniform Cu doping within the RuO_2. Local interpretable model-agnostic explanations (LIME) and shapley additive explanations (SHAP) were employed to elucidate the feature contributions to the OER performance [53,54]. A RF model was trained on the experimental data, achieving LOOCV determination coefficients of R^2 = 0.82 and 0.75, with MSE of 51.3 mV^2 and 84.2 h for overpotential and stability. Both LIME and SHAP analyses were then applied to quantify the influence of synthesis parameters on the predicted catalytic performance. LIME, focusing on local approximations of the predictions, identified the synthesis time and temperature as critical parameters for reducing overpotential and enhancing catalytic activity. In contrast, V_{H_2O} and V_{Ru} exhibited a slight negative impact on activity. However, this trade-off is strategically advantageous: while marginally compromising activity, the optimized V_{H_2O} and V_{Ru} configurations significantly improved catalyst stability, resulting in enhanced durability (Fig. 4f). SHAP analysis further corroborated these findings (Fig. 4g). The color-mapped SHAP values illustrate distinct roles of each parameter. Overpotential reduction was driven by synthesis time and temperature (positive contributions), whereas V_{H_2O} and V_{Ru} increased overpotential (negative contributions). Stability enhancement benefited uniformly from all four parameters (positive contributions). Critically, both LIME and SHAP consistently ranked synthesis time and temperature as the dominant factors influencing performance, followed by V_{Ru} and V_{H_2O}.

This alignment validates the rational design of the Cu-RuO_2 electrocatalyst, demonstrating its optimal balance between activity and stability within the studied chemical system.

5. OER mechanism

To elucidate the origin of the exceptional OER performance of the Cu-RuO_2 catalyst, we conducted a comprehensive investigation of its electronic structure, local atomic configuration, and OER pathway. Comparative X-ray photoelectron spectroscopy (XPS) and X-ray absorption near-edge structure (XANES) analyses were conducted on both Cu-RuO_2 and a commercial RuO_2 reference sample. The Ru 3d XPS spectra (Fig. S15 online) exhibit distinct binding energy shifts in Cu-RuO_2 compared to commercial RuO_2 [6,15,40]. Specifically, the characteristic Ru $3d_{5/2}$ and Ru $3d_{3/2}$ peaks shift from 280.7 and 284.9 eV in commercial RuO_2 to higher values in Cu-RuO_2, suggesting an increase in the Ru oxidation state [6]. This is further supported by Ru K-edge XANES spectra (Fig. 5a), where Cu-RuO_2 displays a positive edge shift and enhanced white line intensity in comparison to commercial RuO_2, manifesting enhanced Ru–O covalency and increased Ru oxidation state, both known to promote OER activity [6,8,55]. The O 1s spectra show the lattice oxygen peak (529.4 eV in commercial RuO_2) shifts to higher binding energy in Cu-RuO_2 (Fig. S16 online), confirming the enhanced Ru–O covalency through Cu doping [6]. Raman spectroscopy reveals further structural modifications (Fig. S17 online). The characteristic Raman peaks at 521, 639, and 701 cm^{-1}, corresponding to the E_g, A_{1g}, and B_{2g} modes of RuO_2, exhibit blue shifts and broadening in Cu-RuO_2, indicating altered phonon vibrations due to symmetry reduction from Cu incorporation and nanoparticle size effects [38,56]. Collectively, these results demonstrate that Cu doping creates a local Ru–O–Cu structure that inhibits the dissolution of Ru, thereby enhancing the OER stability [23].

To elucidate the OER pathway, we conducted operando differential electrochemical mass spectrometry (DEMS) with ^{18}O isotope labeling during CV experiments (see Supplementary material). Fig. 5b, c presents the DEMS results for Cu-RuO_2 and commercial RuO_2 in 0.5 mol L^{-1} H_2SO_4 solution containing $H_2^{16}O$. The measured $^{34}O_2$ (^{16}O + ^{18}O) to $^{32}O_2$ (^{16}O + ^{16}O) signal ratio for both catalysts remains below 2.0 at% [6]. These results confirm the negligible involvement of lattice oxygen in the OER process over both Cu-RuO_2 and commercial RuO_2, supporting an adsorbate evolution mechanism (AEM) pathway ($H_2O \rightarrow OH^* \rightarrow O^* \rightarrow OOH^* \rightarrow O_2$). Therefore, DFT calculations were performed based on the AEM to eluci-

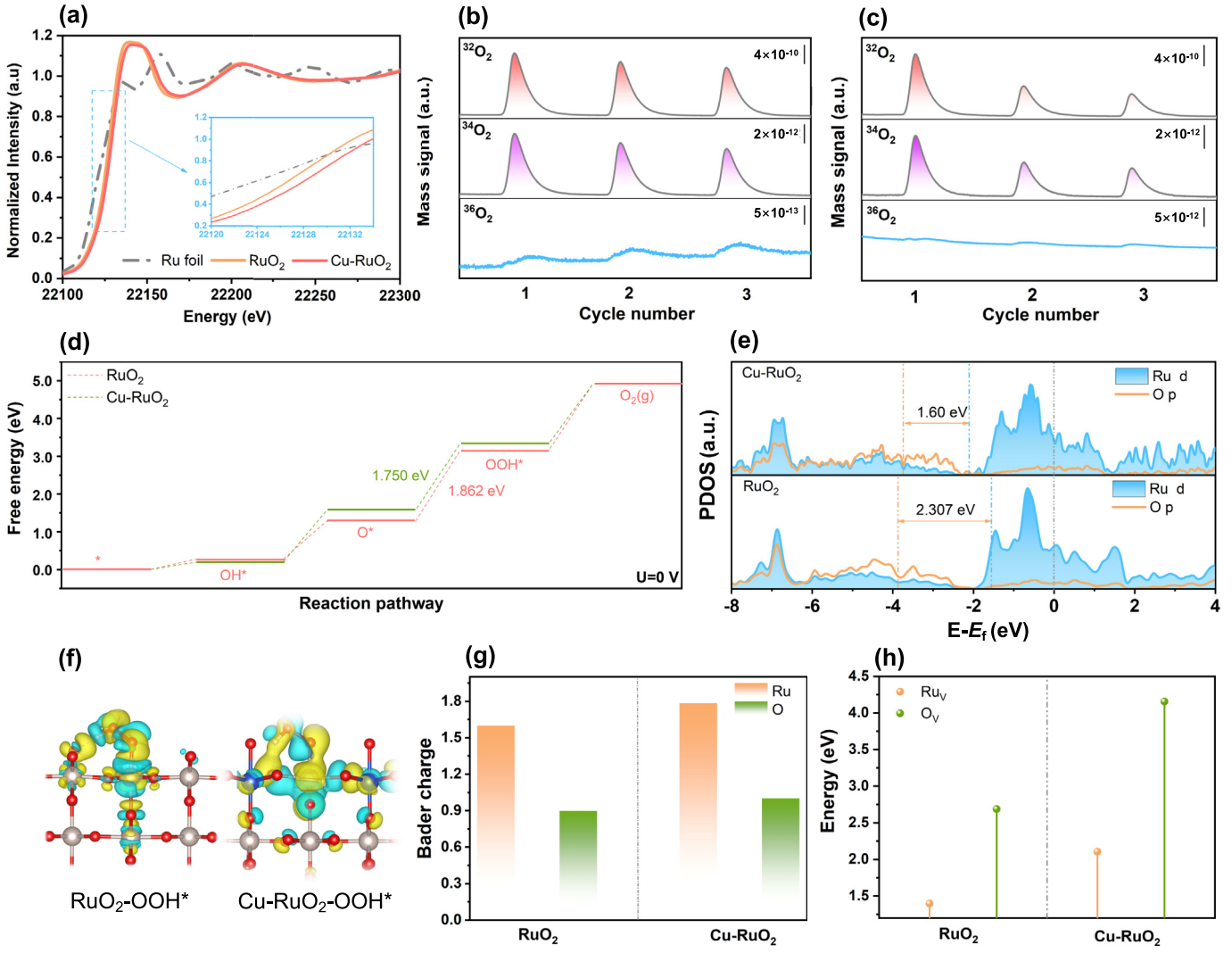

Fig. 5. OER mechanism. (a) Ru K-edge XANES spectra of commercial RuO_2 and Cu-RuO_2. (b, c) DEMS signals of O_2 products for Cu-RuO_2 and commercial RuO_2 in the electrolyte using $H_2^{18}O$ as the solvent during three CV scans in the potential range of 1.00–1.55 V versus RHE, at a scan rate of 5 mV s^{-1}. (d) Obtained OER free-energy diagrams for RuO_2 and Cu-RuO_2. (e) PDOS of Ru d and O p of RuO_2 and Cu-RuO_2. (f) The charge density difference of adsorbed OOH* onto the Ru active site in RuO_2 and Cu-RuO_2. (g) Bader charge of Ru and O in CuO, RuO_2 and Cu-RuO_2. (h) Formation energies of Ru and O vacancies in RuO_2 and Cu-RuO_2.

date how the Cu doping enhances the OER performance. A Cu-RuO_2 slab model was constructed on the most stable (110) surface, with the position of the Cu atom randomly selected (Figs. S18, S19 online) [57]. As revealed in Fig. 5d, the rate-determining step (RDS) for RuO_2 is the O → OOH* transition, exhibiting a Gibbs free energy barrier (ΔG) of 1.862 eV. In contrast, the energy barrier of the RDS for Cu-RuO_2 is reduced to 1.750 eV. These results demonstrate that Cu doping alters the reaction pathway while concurrently lowering the kinetic barrier, thereby enhancing catalytic efficiency. Furthermore, our DFT calculations show that the RPBE functional yields weaker adsorption of small molecules compared to PBE (Fig. S20 and Table S9 online). We also provide projected density of states (PDOS) plots of RuO_2 before and after Cu doping (Fig. 5e). In pristine RuO_2, the Ru d-band center was located at –1.58 eV and the O p-band center at –3.89 eV. Upon Cu doping, the Ru d-band center shifted downward to –2.13 eV, while the O p-band center moved upward to –3.73 eV. This shift of Ru d band center weakens interactions between the Ru active site and oxygen intermediates, rationalizing the reduced energy barrier [23]. This finding is corroborated by the differential charge distribution maps for OOH* in RuO_2 and Cu-RuO_2 (Fig. 5f), which reveal that Cu doping effectively enhances the OER activity by modulating the strength of interactions with adsorbed intermediates.

Furthermore, a comprehensive analysis based on Bader charge (Fig. 5g and Fig. S21 online), charge density distribution maps (Fig. S22 online), and charge density difference maps (Fig. S23 online), of Cu-RuO_2 reveals that Cu donates electrons to O, leading to an increased electron density on O. Simultaneously, this promotes additional electron donation from Ru, thereby enhancing the covalency of Ru–O bonds. This observation aligns with the PDOS results (Fig. 5e), which show that Cu doping brings the orbital centers of Ru and O closer together (Cu-RuO_2: 1.60 eV; RuO_2: 2.307 eV), facilitating the formation of a stable local Cu–O–Ru structure. Subsequently, we performed DFT calculations to evaluate the formation energies of Ru and O vacancies before and after Cu doping (Fig. 5h and Fig. S24 online). The results indicate a significant increase in the formation energies of both Ru and O vacancies after Cu incorporation, directly demonstrating that the local Cu–O–Ru structure effectively enhances the structural stability of RuO_2. A comprehensive set of characterization data, including TEM images, elemental EDS mapping, and XPS spectra of Cu-RuO_2 after the OER process, was collected to probe its structural evolution. As illustrated in Figs. S25, S26 (online), Cu-RuO_2 retains its original morphology and crystal structure after the OER process, with clearly detectable and homogeneously distributed signals of Ru, Cu, and O (Fig. S27 online). Moreover, the Ru 3p XPS spectra show negligible changes in both peak shape and binding energy before and after OER, suggesting the preservation of Ru's electronic structure (Fig. S28 online). These results collectively confirm the exceptional OER stability of Cu-RuO_2 and its great potential for practical application in water electrolysis.

6. Conclusion

In this work, we propose a novel spatial-adaptive active learning strategy to seamlessly integrate ML with experimental synthesis pathways. The CVAE network effectively guides closed-loop experimentation, requiring only 23 synthesized samples and 11 stability tests. This approach eliminates at least 12 additional stability tests, reducing testing time by approximately 4734 h based on the average test duration. As a result, we identify a Cu-RuO_2 catalyst with exceptional stability of 625 h and an overpotential of 177 mV at 10 mA cm^{-2} in an acidic electrolyte. The synergistic combination of experimental characterization and DFT calculations reveals that Cu doping tailors the electronic interaction between Ru active sites and oxygen intermediates, thereby lowering the energy barrier of the rate-determining step. Meanwhile, the Cu–O–Ru bridge structure stabilizes the Ru coordination environment by suppressing Ru dissolution, thus realizing a high-performance Ru-based electrocatalysts.

Conflict of interest

The authors declare that they have no conflict of interest.

Acknowledgments

This work was supported by the National Natural Science Foundation of China (22502040 and 12374003), Shenzhen Basic Research Special Project (Natural Science Fund) Key Basic Research Project (JCYJ20241202123505008), Shenzhen Science and Technology Program (JCYJ20220531095208019 and GXWD20231129103124001), and Guangzhou Municipal Science and Technology Project (2023A03J0003), Guangdong Basic and Applied Basic Research Foundation (2024A1515030256).

Author contributions

Yin Qin, Kaikai Li, and Tong-Yi Zhang managed the project and conceived the storyline of the paper. Bin Cao conducted the modeling and analysis of ML. Yin Qin synthesized the materials and performed the electrochemical and structural characterization and analysis. Yan Luo performed the DFT calculations. Zhehan Ying, Zilin Yan, and Lu-Tao Weng contributed to the discussions of the project.

Data availability

The experimental and computational data generated in this study are provided in the article and the Supplementary Material. The Source codes of Bgolearn is available at https://github.com/Bin-Cao/Bgolearn, and the CVAE package is available at: https://github.com/Bgolearn/VSGenerator.

Appendix A. Supplementary material

Supplementary data to this article can be found online at https://doi.org/10.1016/j.scib.2025.12.021.

References

[1] Fu J, Fan Z, Nakabayashi M, et al. Interface engineering of Ta_3N_5 thin film photoanode for highly efficient photoelectrochemical water splitting. Nat Commun 2022;13:729.
[2] Hu C, Zhang L, Gong J. Recent progress made in the mechanism comprehension and design of electrocatalysts for alkaline water splitting. Energy Environ Sci 2019;12:2620–45.
[3] Seh ZW, Kibsgaard J, Dickens CF, et al. Combining theory and experiment in electrocatalysis: insights into materials design. Science 2017;355:6321.
[4] An L, Wei C, Lu M, et al. Recent development of oxygen evolution electrocatalysts in acidic environment. Adv Mater 2021;33:2006328.
[5] Carmo M, Fritz DL, Merge J, et al. A comprehensive review on PEM water electrolysis. Int J Hydrog Energy 2013;38:4901–34.
[6] Wu ZY, Chen FY, Li B, et al. Non-iridium-based electrocatalyst for durable acidic oxygen evolution reaction in proton exchange membrane water electrolysis. Nat Mater 2022;22:100–8.
[7] Sardar K, Petrucco E, Hiley CI, et al. Water-splitting electrocatalysis in acid conditions using ruthenate-iridate pyrochlores. Angew Chem Int Ed 2014;53:10960–4.
[8] Zhao ZL, Wang Q, Huang X, et al. Boosting the oxygen evolution reaction using defect-rich ultra-thin ruthenium oxide nanosheets in acidic media. Energy Environ Sci 2020;13:5143–51.
[9] Feng Q, Yuan X-Z, Liu G, et al. A review of proton exchange membrane water electrolysis on degradation mechanisms and mitigation strategies. J Power Sources 2017;366:33–55.

[10] Yao Y, Hu S, Chen W, et al. Engineering the electronic structure of single atom Ru sites via compressive strain boosts acidic water oxidation electrocatalysis. Nat Catal 2019;2:304–13.
[11] Shan J, Zheng Y, Shi B, et al. Regulating electrocatalysts via surface and interface engineering for acidic water electrooxidation. ACS Energy Lett 2019;4:2719–30.
[12] Stoerzinger KA, Diaz-Morales O, Kolb M, et al. Orientation-dependent oxygen evolution on RuO_2 without lattice exchange. ACS Energy Lett 2017;2:876–81.
[13] Rossmeisl J, Qu ZW, Zhu H, et al. Electrolysis of water on oxide surfaces. J Electroanal Chem 2007;607:83–9.
[14] Exner KS. Design criteria for oxygen evolution electrocatalysts from first principles: introduction of a unifying material-screening approach. ACS Appl Energy Mater 2019;2:7991–8001.
[15] Lin Y, Tian Z, Zhang L, et al. Chromium-ruthenium oxide solid solution electrocatalyst for highly efficient oxygen evolution reaction in acidic media. Nat Commun 2019;10:162.
[16] Hao S, Liu M, Pan J, et al. Dopants fixation of ruthenium for boosting acidic oxygen evolution stability and activity. Nat Commun 2020;11:5368.
[17] Burnett DL, Petrucco E, Rigg KM, et al. $(M,Ru)O_2$ (M = Mg, Zn, Cu, Ni, Co) rutiles and their use as oxygen evolution electrocatalysts in membrane electrode assemblies under acidic conditions. Chem Mater 2020;32:6150–60.
[18] Chen S, Huang H, Jiang P, et al. Mn-doped RuO_2 nanocrystals as highly active electrocatalysts for enhanced oxygen evolution in acidic media. ACS Catal 2020;10:1152–60.
[19] Tian Y, Wang S, Velasco E, et al. A Co-doped nanorod-like RuO_2 electrocatalyst with abundant oxygen vacancies for acidic water oxidation. Iscience 2020;23:100756.
[20] Zhang L, Jang H, Liu H, et al. Sodium-decorated amorphous/crystalline RuO_2 with rich oxygen vacancies: a robust pH-universal oxygen evolution electrocatalyst. Angew Chem Int Ed 2021;60:18821–9.
[21] Su J, Ge R, Jiang K, et al. Assembling ultrasmall copper-doped ruthenium oxide nanocrystals into hollow porous polyhedra: highly robust electrocatalysts for oxygen evolution in acidic media. Adv Mater 2018;30:1801351.
[22] Meng G, Sun W, Mon AA, et al. Strain regulation to optimize the acidic water oxidation performance of atomic-layer IrO_x. Adv Mater 2019;31:1903616.
[23] Qin Y, Yu T, Deng S, et al. RuO_2 electronic structure and lattice strain dual engineering for enhanced acidic oxygen evolution reaction performance. Nat Commun 2022;13:3784.
[24] Wang J, Xie H, Wang Y, et al. Distilling accurate descriptors from multi-source experimental data for discovering highly active perovskite OER catalysts. J Am Chem Soc 2023;145:11457–65.
[25] Jiang X, Wang Y, Jia B, et al. Using machine learning to predict oxygen evolution activity for transition metal hydroxide electrocatalysts. ACS Appl Mater Interfaces 2022;14:41141–8.
[26] Moon J, Beker W, Siek M, et al. Active learning guides discovery of a champion four-metal perovskite oxide for oxygen evolution electrocatalysis. Nat Mater 2023;23:108–15.
[27] Suvarna M, Zou T, Chong SH, et al. Active learning streamlines development of high performance catalysts for higher alcohol synthesis. Nat Commun 2024;15:5844.
[28] Cherevko S, Zeradjanin AR, Topalov AA, et al. Dissolution of noble metals during oxygen evolution in acidic media. Chemcatchem 2014;6:2219–23.
[29] Hodnik N, Jovanovic P, Pavlisic A, et al. New insights into corrosion of ruthenium and ruthenium oxide nanoparticles in acidic media. J Phys Chem C 2015;119:10140–7.
[30] Feng Q, Zou J, Wang Y, et al. Influence of surface oxygen vacancies and ruthenium valence state on the catalysis of pyrochlore oxides. ACS Appl Mater Interfaces 2020;12:4520–30.
[31] Feng Y-Y, Si S, Deng G, et al. Copper-doped ruthenium oxide as highly efficient electrocatalysts for the evolution of oxygen in acidic media. J Alloy Compd 2022;892:162113.
[32] Cao B, Su T, Yu S, et al. Active learning accelerates the discovery of high strength and high ductility lead-free solder alloys. Mater Des 2024;241:112921.
[33] Hernández-Lobato JM, Hoffman MW, Ghahramani Z. Predictive entropy search for efficient global optimization of black-box functions. Adv Neural Inform Process Syst 2014;27:918–26.
[34] Qin C, Klabjan D, Russo D. Improving the expected improvement algorithm. Adv Neural Inform Process Syst 2017;30:5387–97.
[35] Frazier PI, Powell WB, Dayanik S. A knowledge-gradient policy for sequential information collection. SIAM J Control Optim 2008;47:2410–39.
[36] Chawla NV, Bowyer KW, Hall LO, et al. Smote: synthetic minority over-sampling technique. J Artif Intell Res 2002;16:321–57.
[37] Van der Maaten L, Hinton G. Visualizing data using *t*-SNE. J Mach Learn Res 2008;9:2579–605.
[38] Wang Y, Yang R, Ding Y, et al. Unraveling oxygen vacancy site mechanism of Rh-doped RuO_2 catalyst for long-lasting acidic water oxidation. Nat Commun 2023;14:1412.
[39] Lin C, Li J-L, Li X, et al. *In-situ* reconstructed Ru atom array on α-MnO_2 with enhanced performance for acidic water oxidation. Nat Catal 2021;4:1012–23.
[40] Hao S, Liu M, Pan J, et al. Dopants fixation of Ruthenium for boosting acidic oxygen evolution stability and activity. Nat Commun 2020;11:118605.
[41] Wang J-Q, Xi C, Wang M, et al. Laser-generated grain boundaries in Ruthenium nanoparticles for boosting oxygen evolution reaction. ACS Catal 2020;10:12575–81.
[42] Jin H, Choi S, Bang GJ, et al. Safeguarding the RuO_2 phase against lattice oxygen oxidation during acidic water electrooxidation. Energy Environ Sci 2022;15:1119–30.
[43] Wang Z, Xiao B, Lin Z, et al. *In-situ* surface decoration of RuO_2 nanoparticles by laser ablation for improved oxygen evolution reaction activity in both acid and alkali solutions. J Energy Chem 2021;54:510–8.
[44] Liu C, Jiang Y, Wang T, et al. Nano Si-doped ruthenium oxide particles from caged precursors for high-performance acidic oxygen evolution. Adv Sci (Weinh) 2023;10:e2207429.
[45] Shan J, Ling T, Davey K, et al. Transition-metal-doped RuIr bifunctional nanocrystals for overall water splitting in acidic environments. Adv Mater 2019;31:1900510.
[46] Yao Q, Huang B, Xu Y, et al. A chemical etching strategy to improve and stabilize RuO_2-based nanoassemblies for acidic oxygen evolution. Nano Energy 2021;84:105909.
[47] Gao J, Xu C-Q, Hung S-F, et al. Breaking long-range order in iridium oxide by alkali ion for efficient water oxidation. J Am Chem Soc 2019;141:3014–23.
[48] Yang L, Yu G, Ai X, et al. Efficient oxygen evolution electrocatalysis in acid by a perovskite with face-sharing IrO_6 octahedral dimers. Nat Commun 2018;9:5236.
[49] Diaz-Morales O, Raaijman S, Kortlever R, et al. Iridium-based double perovskites for efficient water oxidation in acid media. Nat Commun 2016;7:12363.
[50] Linsey C, Seitz CFD, Nishio K, Hikita Y, et al. A highly active and stable IrO_x/$SrIrO_3$ catalyst for the oxygen evolution reaction. Sepiember 2016;353:1011–4.
[51] Sun SC, Jiang H, Chen ZY, et al. Bifunctional WC-supported RuO_2 nanoparticles for robust water splitting in acidic media. Angew Chem Int Ed Engl 2022;61:e202202519.
[52] Kim J, Shih P-C, Tsao K-C, et al. High-performance pyrochlore-type yttrium ruthenate electrocatalyst for oxygen evolution reaction in acidic media. J Am Chem Soc 2017;139:12076–83.
[53] Lundberg SM, Lee S-I. A unified approach to interpreting model predictions. Adv Neural Inform Process Syst 2017;30:4768–77.
[54] Ribeiro MT, Singh S, Guestrin C. "Why should I trust you?" Explaining the predictions of any classifier. In: In: Proceedings of the Proceedings of the 22nd ACM SIGKDD international conference on knowledge discovery and data mining. p. 1135–44.
[55] Wu Z-Y, Ji W-B, Hu B-C, et al. Partially oxidized Ni nanoparticles supported on Ni-N Co-doped carbon nanofibers as bifunctional electrocatalysts for overall water splitting. Nano Energy 2018;51:286–93.
[56] Wang Y, Li H, Zhou W, et al. Structurally disordered RuO_2 nanosheets with rich oxygen vacancies for enhanced nitrate electroreduction to ammonia. Angew Chem Int Ed Engl 2022;61:e202202604.
[57] Qiu L, Zheng G, He Y, et al. Ultra-small Sn-RuO_2 nanoparticles supported on N doped carbon polyhedra for highly active and durable oxygen evolution reaction in acidic media. Chem Eng J 2021;409:128155.